The Limerick bubbly flow rig: design, performance, hold-up and mixing pattern

Journal Pre-proof

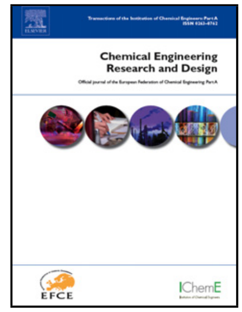

The Limerick Bubbly Flow Rig: Design, Performance, Hold-up and Mixing Pattern

Corné Muilwijk Harry E.A. Van den Akker

PII: S0263-8762(19)30438-1

DOI: https://doi.org/doi:10.1016/j.cherd.2019.09.021

Reference: CHERD 3811

To appear in: *Chemical Engineering Research and Design*

Received Date: 27 March 2019

Revised Date: 12 September 2019

Accepted Date: 19 September 2019

Please cite this article as: Corné Muilwijk, Harry E.A. Van den Akker, The Limerick Bubbly Flow Rig: Design, Performance, Hold-up and Mixing Pattern, *<![CDATA[Chemical Engineering Research and Design]]>* (2019), doi: https://doi.org/10.1016/j.cherd.2019.09.021

The Limerick Bubbly Flow Rig: Design, Performance, Hold-up and Mixing Pattern.

Corné Muilwijk[a,*], Harry E.A. Van den Akker[a,b]

[a] *Bernal Institute, University of Limerick, V94 T9PX, Limerick, Ireland*
[b] *Transport Phenomena Lab, Department of Chemical Engineering, Delft University of Technology, Van der Maasweg 9, 2629 HZ Delft, The Netherlands*

Abstract

As Euler-Euler CFD simulations of bubbly flows suffer from uncertainties due to the many underpinning models, there is an obvious need of accurate experimental data for validation. With this in mind, a new bubbly flow test rig was built to be operated with and without liquid co-flow, with bubble size as uniform as possible in the range 4-7 mm, and with a very even horizontal bubble distribution. We designed the gas sparging system such that we can also produce an essentially bi-modal bubble size distribution. The column consists of two square sections to allow for studying the mixing of two originally separated bubbly flows with either the same or a different bubble size. The bubbles are produced from 2 × 196 needles, bubble sizes are determined with high-speed imaging and with a simple acoustical method, overall volume fractions in the column by means of air chamber pressure measurements. Overall volume fractions are presented as a function of gas and liquid flow rates, with slip velocity mostly increasing with increasing void fraction. First results are obtained on (a) producing bi-model bubble size distributions and the pertinent volume fractions in the column, and (b) flow patterns in the case of unequal aeration.

Keywords: Bubble column design, Multi-needle sparger, Bubble formation, Bi-modal bubble size, Gas hold-up, Mixing pattern

1. Introduction

Gas-liquid flows are widely encountered in the process and (bio)chemical industries in e.g., bubble columns, air-lift reactors and aerated stirred vessels. Companies are interested in a reliable computational fluid dynamics (CFD) technique to explore the effects of e.g. operating conditions, gas sparger design, bubble size, and column or vessel geometry. Given the usually high volume fractions of gas in such industrial gas-liquid systems, computational simulations are often of the Reynolds Averaged Navier-Stokes (RANS) based Euler-Euler type rooted in mutually interpenetrating two fluid modelling.

Such simulations exploit various, often complex, models for the liquid-bubble interaction forces (drag, lift, virtual mass), for the lateral dispersion of the bubbles, and for the turbulent-flow conditions. Sometimes bubble induced turbulence is taken into account [1], in other cases it is ignored. In most, or all, of these models, bubble size is an important parameter [1, 2, 3]. Usually, a single bubble diameter has to be specified in such simulations, or the simulations have to be extended with complex and complicating population balance models (to deal with dynamic real-life bubble size distributions) such as the MUSIG model [4, 5]. And all the above models comprise many model parameters the disputable values of which add to the uncertainty of the simulation results. Many researchers have contributed to the development of improved models and have presented and compared results obtained by various codes exploiting various models [3, 6, 7, 8, 9, 10, 11, 12, 13]. The review by Dhotre et al. [14] is about large eddy simulations of dispersed bubbly flows which suffer from similar modelling issues.

Even recent authors have stressed [1, 15, 16] that there is a need of accurate and reliable experimental data for validating such multiphase (Euler-Euler) CFD simulations. We now have constructed a bubbly flow test rig allowing for the acquisition, for validation purposes, of precise experimental data under meticulously described conditions amenable for reproduction in CFD simulations. The idea is to create bubbly flows with and without liquid co-flow, with a bubble size as uniform as possible, and with a very even bubble distribution across the horizontal cross-section at the base of the column. This mimics computational simulations with a single bubble size and an even gas supply over the cross-section of the column bottom. The advantage of these features when common to experiments and simulations is that it disentangles the effects of bubble size distribution and uneven gas sparging from effects due to liquid-bubble interaction forces and two-phase flow turbulence. This way, we avoid (in a non-coalescing system) the need of population balances.

Additionally, we designed the gas sparging system such that we can also produce an essentially bi-modal bubble size distribution homogeneously distributed over the col-

*Corresponding author

umn base, with no coalescence taking place. In the latter case, a very simple population balance may suffice.

Furthermore, the column is rectangular (facilitating optical accessibility) and consists of two square sections, each with its own gas and liquid supply system, while the two bubbly flows (with the same or a different bubble size) may mix from a certain distance above the gas distributors. The latter feature may allow for validating interaction and lateral mixing of different bubbly flows, e.g. such as in inhomogeneously aerated bubble columns [17], and for studying the dynamics of self-organizing vortical structures [18, 19]. Just a few studies have been performed on (lateral) mixing of bubbly flows [20, 21, 22, 23, 24], but in most cases the bubbles were small and/or the monodispersity was poor.

In designing our test rig, we made use of results reported in our recent paper [25] on bubble formation from a single needle with and without liquid co-flow. In addition, we were guided by the design of previously reported bubble columns [21, 24, 26, 27, 28] (see Table 1). Compared to these earlier designs, we produce larger bubbles which may be industrially more relevant, at least in aqueous systems (in organic liquids, bubbles are usually smaller). Another feature of using larger bubbles is that the rise velocity of individual gas bubbles in the range 4-7 mm is rather constant, viz. 23.5-24.5 cm/s [29]. As a result, bubbles with a slightly deviating size may still rise at more or less the same speed as the bubbles with the nominally uniform size as predicted by our correlation.

This paper describes the design and performance of the novel Limerick Bubble Rig ('LimBuRig') as well as the first experimental findings. The main characteristics of LimBuRig are as follows:

- A transparent bubbly flow channel of size 400×200×2400 mm.
- Superficial gas velocity U_{sg} up to 0.0625 m/s.
- Superficial liquid velocity U_{sl} up to 0.5 m/s.
- Void fractions up to 25 % in the absence of co-flowing liquid.
- Accurate needle spargers capable of producing either a uniform or a bi-modal bubble size distribution.
- Lateral mixing of two parallel bubbly flows with different U_{sg} and/or U_{sl}.

The structure of this paper is as follows. A detailed description of the test rig is presented in Sec. 2. Sec. 3 introduces the experimental techniques used: high-speed imaging and acoustic measurements for determining bubble sizes, and gas chamber pressure measurements with the view of overall void fractions in the column. The performance of the bubble sparger is analyzed in Sec. 4, while overall void fraction data for uniformly aerated conditions - acquired by both the above gas chamber pressure measurements and more common bed expansion measurements - are discussed in Sec. 5. In Sec. 6, first results are reported for cases of bi-disperse bubble size distributions as well as for uneven aeration conditions. Finally, we present our conclusions and future plans.

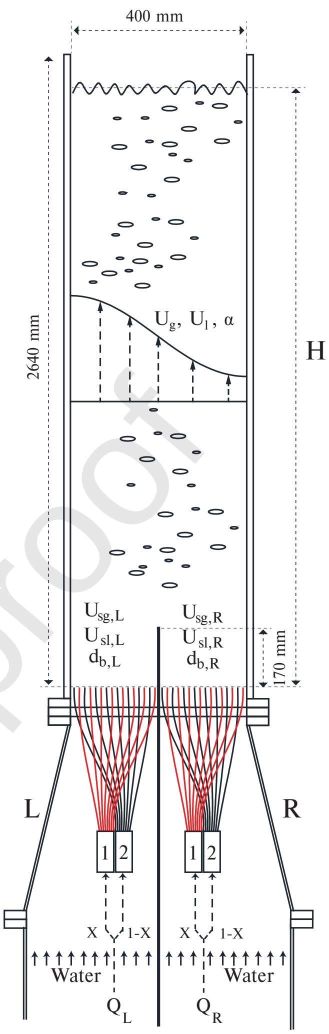

Figure 1: (Color online) Schematic drawing of the test setup where two parallel bubbly streams of air/water flow are mixed in the test channel after the trailing edge of a splitter plate. Both inlets - Left (L) and Right (R) - are seeded with bubbles from two separated (1,2) air chambers (four in total), denoted by chamber L1,R1 (red), and R2,L2 (black). The top of the channel is a free surface and overflowing water is collected and recirculated. α: void fraction; U_{sg}: superficial gas velocity; U_{sl}: superficial liquid velocity; U_g: gas velocity; U_l: liquid velocity; H: level height; d_b: bubble diameter; Q: gas flow rate; X: split ratio.

2. Description of the test rig

2.1. Geometry and dimensions

Fig. 1 shows a schematic drawing of the test facility named LimBuRig, which stands for Limerick Bubble Rig.

It shows two compartments in the lower column section creating two separate bubbly flows, which start interacting downstream of the trailing edge of a splitter plate, with variable superficial gas velocities left (L) and right (R) – denoted by $U_{sg,L}$ and $U_{sg,R}$ – and variable liquid velocities left and right $U_{sl,L}$ and $U_{sl,R}$. The superficial gas and liquid velocities are defined as the volumetric flow rates to

Table 1: Dimensions and characteristics, operating conditions and characteristics of similar bubbly flow columns.

Facility	Dimension [m]	$U_{sl,max}$ [m/s]	$U_{sg,max}$ [m/s]	α_{max} [%]	Sparger type	Liquid flow
Present	0.4×0.2×2.4	0.5	0.0625	25	Needle	Co-current
Drahoš et al. [30]	⌀0.14×4.2		0.126	33	Perforated plate	Batch
Groen et al. [18]	⌀0.152×1.52 ⌀ 0.23×1.87		0.07	30	Perforated plate	Batch
Mudde et al. [31]	⌀0.15×2.0		0.094	55	Needle	Batch
Sharaf et al. [32]	⌀0.127×2.0		0.17	35	Perf. plate & Spider	Batch
Lau et al. [33]	0.20×0.03×1.0		0.03	8.3	Needle	Batch
Alméras et al. [17]	0.15×0.3×1.0		0.03	15	Needle	Batch
Lance and Bataille [27]	0.45×0.45×2.0	1.2		5	Needle	Co-current
Pjontek et al. [34]	⌀0.102×1.8	0.9	0.15	35	Porous tube	Co-current
Magaud et al. [35]	0.3×0.1×4.0	0.125	0.07	18	Spider	Co-current
Krepper et al. [36]	0.1×0.02×1.45		0.02	8.5	Porous tube	Batch
Lau et al. [37]	⌀0.14×1.5		0.108	30	Perforated plate	Batch
Medjiade et al. [38]	⌀0.102×2.4		0.175	25	Perforated plate	Batch
Simonnet et al. [39]	0.1×0.1×1.0	0.1	0.08	35	Needle	Co-current
Letzel et al. [40]	⌀0.15×1.22		0.4	65	Perforated plate	Batch
Thorat et al. [41]	⌀0.385×3.2		0.3	33	Perforated plate	Batch
Twente Water Tunnel[26, 42]	0.45×0.45×2	0.9	0.008	10	Needle islands	Co/counter-current
Roig et al. [21]	0.4×0.4×2	1		5	Porous tube	Co-current
De Tournemine and Roig [24]	0.3×0.15×3.1	1.3	0.1	25	Needle	Co-current
Besagni et al. [43]	⌀ 0.24×5.3	-0.09	0.2	26	Spider	Co/counter-current

an inlet compartment (at standard pressure) divided by its cross-sectional area (200×200 mm).

The height of the flow channel above the trailing edge of the splitter plate is 2470 mm and a free surface is created on top of the flow channel with symmetric overflow to all sides. The width of the channel is 400 mm and the depth (not shown) is 200 mm. Bubbles are formed by a needle sparger, which is further discussed in Sec. 2.2, 170 mm below the trailing edge of the splitter plate. Fig. 2a shows a 3D CAD drawing of the test facility. The test section (No. 12) is made of 15 mm thickness polycarbonate sheet and access ports are drilled every 200 mm in the sides of the flow channel to facilitate installation of measurement probes.

Two centrifugal pumps (No. 1) with variable speed drive are installed to provide constant circulation of water at a liquid flow rate up to 0.02 $m^3/s \equiv 72\ m^3/h$. Two DN100 Krohne Eletromagnetic flowmeters (No. 2) are installed to measure the liquid flow rates. The flow rate can be further adjusted by manual operation of the butterfly valves (No. 3). Flow reversal is prevented through installation of swing check valves (No. 4).

Two stainless steel expanders (No. 5) to enlarge DN100 to DN300 are connected to the inlet (No. 7) and a blanking flange with bore-through fittings (No. 6) is mounted to the secondary DN100 inlet of the expanders to connect the air supply for the needle spargers.

Corner vanes are installed in the bend (No. 8) with a mutual spacing of 50 mm to reduce large turbulent flow structures. The cross-sectional area of the vertical duct is 600×400 mm with a splitter plate (No. 11) in the middle to create two separate channels of 300×400 mm.

A stainless steel calming chamber (No. 9) of height 600 mm is equipped with two polycarbonate honeycombs in each channel of 100 mm thickness and ⌀3 mm cell size.

A stainless steel contraction (No. 10) of height 700 mm was installed to reduce the cross-sectional area (contraction ratio is 3) to meet the size of the inlet of the test channel. The outlet of the contraction is 400 × 200 mm, resulting in two square flow channels of 200 × 200 mm.

A fiberglass vessel (No. 13) of 686 × 510 × 510 mm is used as overflow vessel. A 200 mm high 200 mm × 400 mm extension of the flow channel was made out of 10 mm plastic sheet and fitted in the center of the vessel in order to create a free surface (No. 14) on top of the test channel and well above the outlet pipe. Water is recirculated to the 2000 L buffer vessel (No. 17) via a 150 mm drain pipe (No. 16), while air is vented by the air outlet (No. 15).

The buffer vessel is equipped with two DN100 connections (not visible in Fig. 2a) and connected to the pump inlets. Filtered tap water (Everpure Claris Ultra 2000-XXL filter) was stored in this vessel and was refreshed at least once per month.

2.2. Air sparging

An overview of some needle spargers used by others is given in Tab. 2. In these cases a large amount of needles was required in order to create a bubbly flow with a uniform bubble size distribution. Fig. 2b,2c show an assembly

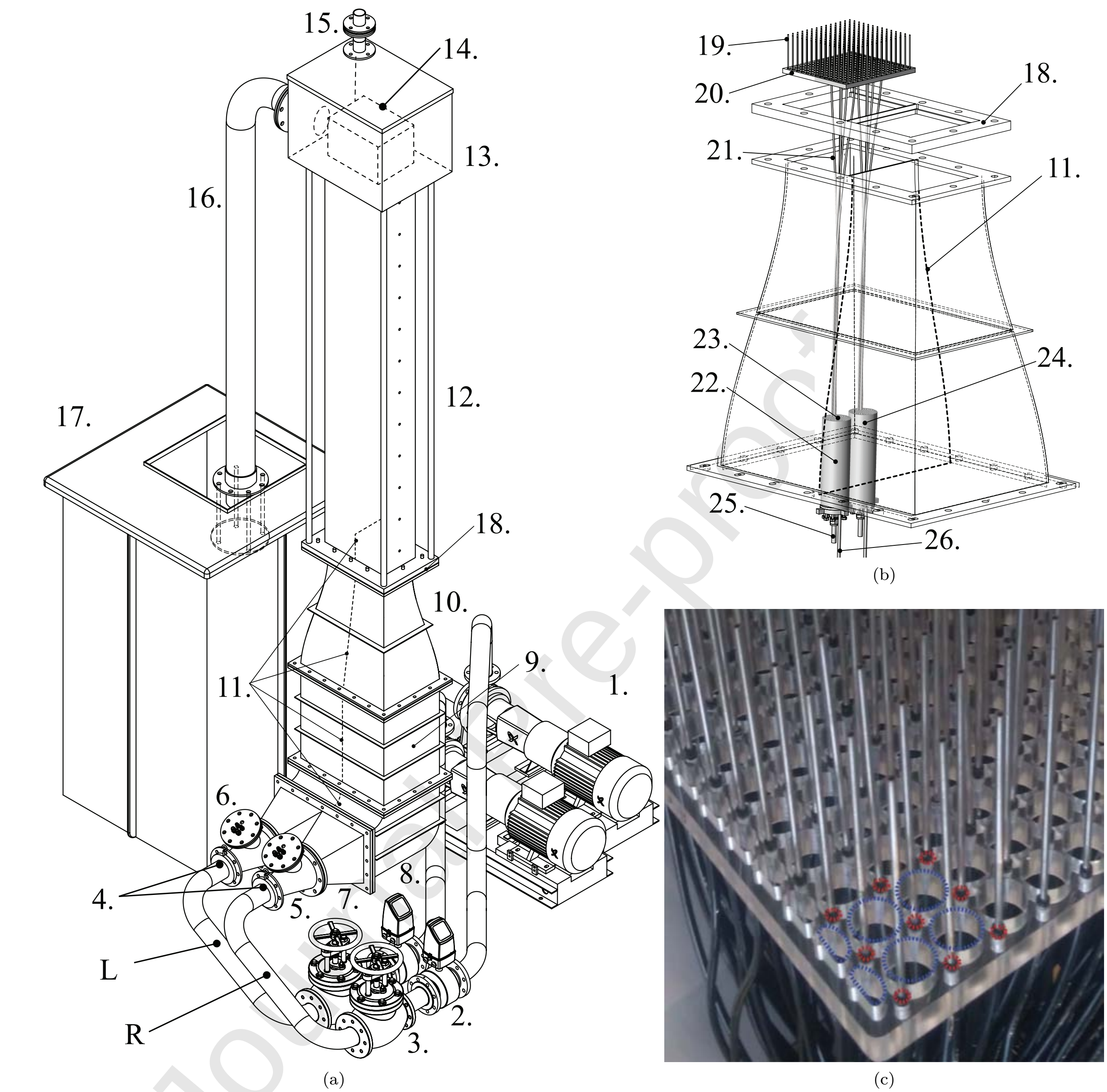

Figure 2: (a) Assembly of the test rig. 1) pumps; 2) electromagnetic flow meters; 3) butterfly valves; 4) wafer swing check valves; 5) expanders; 6) air supply connections; 7) inlet; 8) bend; 9) calming chamber; 10) contraction; 11) splitter plate; 12) test channel; 13) overflow vessel; 14) free surface; 15) air vent; 16) return pipe; 17) buffer vessel; L) Left side inlet; R) Right side inlet. (b) Assembly of the spargers (only left sparger shown for clarity). 18) grid holder; 19) ⌀ 1.55 mm i.d. needles; 20) perforated grid; 21) flexible tubes (only a few flexible tubes are drawn for clarity); 22) air chambers; 22) distributor caps; 24) inserted capillaries; 25) air supply tubes (9.5 mm o.d.); 26) probe/drain tubes (6.4 mm o.d.). (c) Close up photograph of a perforated needle grid. The small red circles mark the small boreholes to mount the needles; the large blue circles (⌀ 13 mm) mark the openings for the water flow.

and a close-up photograph of one of the two spargers we constructed, which we will discuss below.

2.2.1. Perforated needle grid

Based on our previous study of bubble formation from a single nozzle [25], we decided to install 1.55 mm inner diameter needles, which are rather large (compared to the study of De Tournemine and Roig [24]), to facilitate the formation of (almost) uniformly sized bubbles in the range 4 - 7 mm in volume equivalent diameter.

In each compartment (left and right), a perforated grid (No. 20) comprises 14×14 (=196) straight cut stainless

Table 2: Needle dimensions and flow rates for previously reported needle spargers. d_i: inner diameter and L length in mm.

Facility	No. of needles	Needle size $d_i \times L$ [mm]	Q_n [cm^3/s]
Present	2×196	1.55×75	0.6 - 12.6
De Tournemine and Roig [24]	2×576	0.33×800	0 - 14.5
Poorte and Biesheuvel [26]	(9×69) 621	0.5×50	0 - 2.7
Mudde et al. [31]	559	0.8×200	1 - 3
Alméras et al. [17]	1800	0.2	0.125-0.75
Lau et al. [33]	20	1.0	1.5-9
Simonnet et al. [39]	133	0.44×180	0-6

steel needles of 1.55×2.05×75 mm (No. 19), in a square array at a spacing of 14.4 mm (marked red in Fig. 2c). By doing so, we compromised between the number of needles (construction feasibility) and needle flow rate (pressure drop, single bubble detachment). Air is supplied to each needle by 1.69×3.18×800 mm polyurethane tubes (No. 21). In between each set of 4 needles, a 13 mm borehole (see blue dashed circles) allows for water flowing through the grid into the column. These needle grids are kept in place by a flanged grid holder (No. 18) and the open area for the water flow amounts to 64 %.

Based on an experimental and numerical study of Rana et al. [44, 45], the bubble formation of the neighboring nozzle is assumed to have a negligible effect on the bubble formation as the nozzle-to-nozzle distance is quite large (14.4 mm) compared to the bubbles formed and coalescence between two nozzles is very unlikely.

Fig. 1 and 2b show that the two compartments left and right each contain two identical air chambers (No. 22), which are indicated by L1,L2 (Left) and R1,R2 (Right). The needles in a grid (196) are fed from two air chambers, such that two neighbouring nozzles are always connected to a different chamber. This is explained in Fig. 3. Hereby, we create the option of producing a homogeneously distributed bi-disperse bubble mixture by supplying a different gas flow rate to each chamber – which is different than in the facility of Poorte and Biesheuvel [26] and De Tournemine and Roig [24].

2.2.2. Air chambers

The body of such an air chamber (No. 22) is made out of ⌀ 63 mm plastic pipe with a length of 225 mm and 98 tubes are connected to the top of each chamber using special made distributor caps with 98 perforations (No. 23).

For a proper functioning of a distributor, where the flow has to be equally distributed over 98 streams, it is important that the pressure drop characteristics (e.g. diameter, length) over each of those outlets is similar. Therefore, small capillaries of 0.46×1.59× 50 mm were inserted in the polyurethane tubes (indicated by No. 24). These capillaries increase the pressure drop in order to allow lower flow rates without the occurrence of weeping (or gas maldistribution [46]) for the following reasons: (1) to improve the gas distribution across the 98 needles per chamber to ensure that every needle receives the same flow rate (see also Appendix A.1) and emits bubbles at a similar rate and (2) to increase the pressure ratio PR, which is defined in Muilwijk and Van den Akker [25] as a ratio of the surface tension pressure to the pressure drop over the nozzle, to operate under constant flow condition and therefore, reducing the weep point.

Two Bronkhorst EL-FLOW F202AV mass flow controllers, with accuracy ratings of ± 0.5 % of the reading ± 0.5 % of the full scale of 150 L/min, are installed to regulate the gas flow for each compartment, denoted by Q_L and Q_R in Fig.1. Each regulated air flow is then further divided over two streams and air is supplied to the chambers by 6.35×9.5 mm ×5.4 m polyurethane tubes (No. 25) which are connected to the bottom of the air chambers. The flow rate to each chamber Q_{ch} is measured by rotameters and the gas flow rate per needle, Q_n, is then calculated from the gas flow rate to an air chamber divided by 98 needle outlets.

Under normal operation, the regulated air flows are equally divided over two chambers (split ratio X= 50%, see Fig. 1), whereas the split ratio can be further adjusted by manual gate valves in order create a bi-disperse bubble size distribution ($X \neq 50\%$).

The pressures in all four chamber P_{ch} are continuously monitored by digital (Honeywell ABPDANT005PGAA5) pressure sensors, with an accuracy rating of 0.25 % of the full scale (345 mbar), which are connected to the bottom of the pressurized chambers by smaller 3.18×6.35 mm×3 m polyurethane tubes (No. 26). In addition, this tubes may act as a drain of the pressurized chambers in case weeping has occurred and water has penetrated the needles and entered the chambers.

3. Experimental techniques

3.1. Measurements of bubble formation rates and diameters

In order to assess the performance of the sparger and to obtain the bubble size distribution, bubble formation rates of the (multi-needle) gas sparger are measured as function of superficial gas velocity U_{sg}, and liquid co-flow

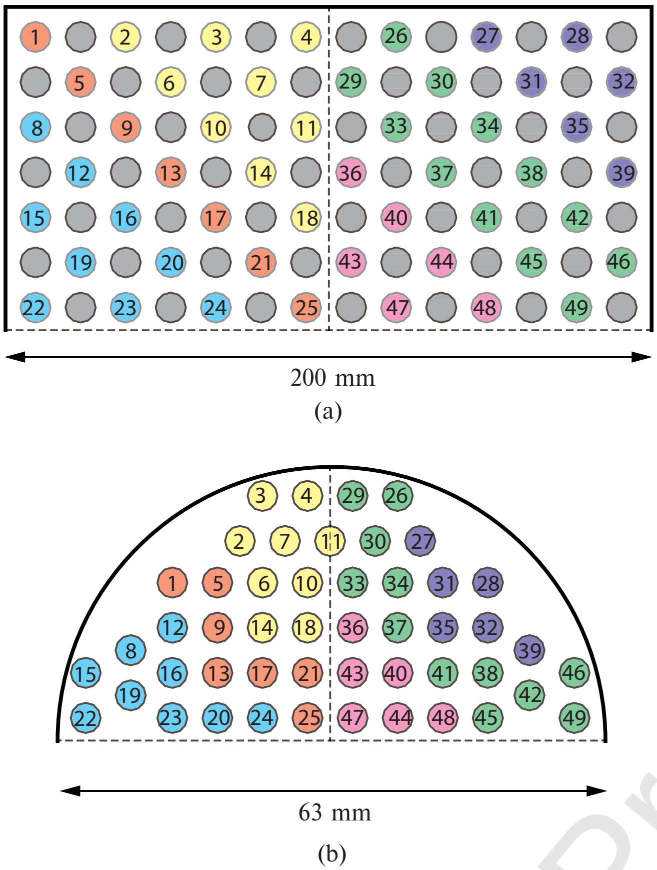

Figure 3: Layout of the needles in the grid (a) and the connections to a corresponding distributor (b). The ⌀ 13 mm holes for the water flow are not shown. The colored needle positions denote the connections to one air chamber, whereas the gray needle positions (not numbered) are connected to the other air chamber (which is not shown). The different colors are drawn as a guide for the eye. Only the colored upper halves (a,b) are numbered as the connection pattern is rotationally symmetric.

velocity U_{sl} by high-speed imaging analysis and acoustic measurements.

The average bubble equivalent diameter can be derived from the needle gas flow rate Q_n, and the measured bubble formation rate f_b, according to:

$$d_b = \left(\frac{6Q_n}{\pi f_b}\right)^{1/3} \tag{1}$$

Typical photographs of the bubble formation on the sparger are given in Fig. 4 for three different air and water flow rates. Images of the bubble formation were recorded with a IDT X-Stream XS-4 camera (using a 0.75–5× microscopic video zoom lens assembly) at a resolution of 512×512 pix and at a rate of 200-400 Hz for 10 seconds, while the column was illuminated with a continuous LED light from the left. Bubble formation rates are obtained by monitoring pixel intensities in the vicinity of orifice outlets (≈ 5 pix left and ≈ 10 pix above nozzle outlets), where we observe cyclic patterns of highly reflective bubble interfaces passing through the monitored pixels. In each set of images, up to 30 needle outlets could be monitored simultaneously.

For the acoustic measurements, one of the pressure sensors (connected to chamber L1) was removed and a waterproof microphone (Micronic, Primo EM121, ⌀ 8 mm with 2-stage pre-amplifier) was connected to the probe tube (No. 26 in Fig. 2b). The microphone response signal (in Volts) was recorded for 30 s at a rate of 20 kHz. The signal was divided in eleven blocks of 5 s, with an overlap of 50 %, and multiplied with the Hanning function. The Fast Fourier Transforms were computed for these blocks and averaged in the frequency domain to obtain the bubble formation rate. This procedure was repeated for several gas flow rates as shown in Fig. 5.

3.2. Bed expansion measurements

For the bed expansion experiments, the column was filled with a fixed amount of water while the superficial gas velocity was kept at a value >0.01 m/s. The superficial gas velocity was varied in the range 0.004-0.0625 m/s and the water level height H (above the needle outlets) was measured as a function of the superficial gas velocity U_{sg} by means of a measuring tape with an accuracy of ± 2 mm at low superficial gas velocities and ± 2 cm at high superficial gas velocities. The gas hold-up α_b, obtained from the bed expansion measurements, was then calculated according to:

$$\alpha_b = \frac{H - H_0}{H} \tag{2}$$

where H_0 is the liquid height at zero aeration. This procedure was repeated for various liquid loadings (H_0).

3.3. Chamber pressure measurements

In order to measure the overall gas hold-up in the bubble column, we postulate that the gauge pressure in each air chamber P_{ch} is the summation of the hydrostatic pressure P_H, the Laplace pressure ΔP_{LP} and the distributor pressure drop $\Delta P_{d,ch}$. The needle outlet pressure P_{no} can then be described by:

$$P_{no} = P_{ch} - \Delta P_{d,ch} = P_H + \Delta P_{LP} \tag{3}$$

where

$$\Delta P_{LP} \approx \frac{4\sigma}{d_n} \tag{4}$$

and

$$P_H = \rho_w g(H - d_b) \times (1 - \alpha) \tag{5}$$

where σ is the surface tension of water/air, d_n the nozzle diameter, d_b the bubble diameter, g the gravitational constant, ρ_w the water density, H the height of the free surface above the nozzle outlets and α the void fraction. Chamber pressures P_{ch} were recorded simultaneously with the bed height H as a function of the gas flow rate setting and the void fraction α_p can then be calculated according to:

$$\alpha_p = 1 - \frac{P_{ch} - \Delta P_{d,ch} - \Delta P_{LP}}{\rho_w g(H - d_b)} \tag{6}$$

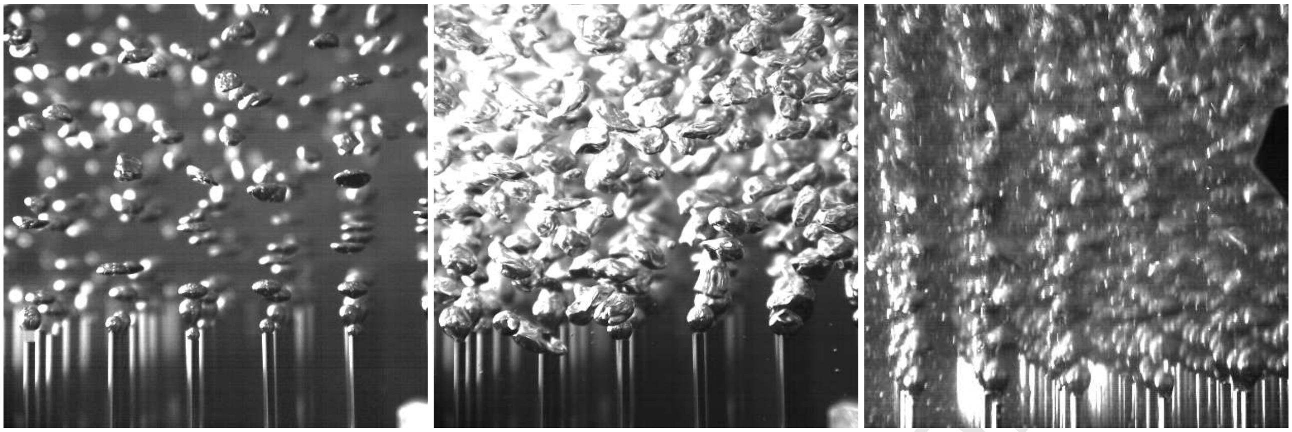

(a) $U_{sg} = 0.38$ cm/s,
$Q_n = 0.77$ cm^3/s,
$U_{sl} = 0$ m/s

(b) $U_{sg} = 2.5$ cm/s,
$Q_n = 5.1$ cm^3/s,
$U_{sl} = 0$ m/s.

(c) $U_{sg} = 2.5$ cm/s,
$Q_n = 5.1$ cm^3/s,
$U_{sl} = 0.3$ m/s.

Figure 4: Photographs of the sparger taken with a high-speed camera. Illumination is from the left. The corresponding videos can be found in the Supplementary Material.

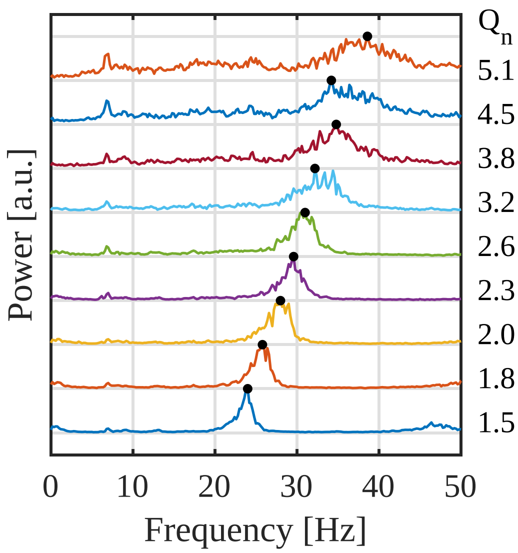

Figure 5: Fast Fourier transforms of the microphone response signal for various Q_n. The signals are acquired from air chamber L1. Q_n in cm^3/s.

The distributor pressure drops $\Delta P_{d,ch}$ were measured as a function of the gas flow rate and shown in Fig. A.13 in Appendix A.1. Both H and ΔP_d (varying with gas flow rate) are required for Eq. (6). In spite of the need of these two parameters, Eq. (6) is very useful to calculate α when the bed expansion method cannot be used (for bubble columns with co-flowing liquid), or when H_0 could not be determined.

4. Sparger performance

4.1. Bubble formation from a single submerged needle

Due to the use of small capillaries inserted in the air supply tubes, a constant gas flow rate condition is imposed. We carried out a new series of experiments in the single needle test setup described in Ref. [25] (where bubbles were formed under a constant pressure condition) but now with a similar capillary restriction inserted.

Bubble formation rates, without liquid co-flow, were measured using a microphone connected to the pressurized chamber and the gas flow rate Q_n (corrected for the density change due to hydrostatic pressure) was varied in the range 0.01-4.0 cm^3/s.

Fig. 6a shows the resulting bubble diameter as a function of the needle gas flow rate. The imposed constant flow condition results in smaller bubbles at low/intermediate flow rates as compared to the prediction of Muilwijk and Van den Akker [25].

The weep point drastically reduced, as compared to our previous study [25], to a flow rate well below a critical flow rate, where bubbles detach with a constant volume [47]. In this quasi-static flow regime, when buoyancy ($\frac{\pi}{6}\rho_g g d_b^3$) and surface tension ($\sigma d_n$) are in equilibrium, the theoretical bubble size of bubbles formed on a 1.55 mm inner diameter needle is 4.1 mm, which agrees very well with our findings.

We also compared our data to the correlation proposed by Gaddis and Vogelpohl [48]. We observe good agreement at low/high flow rates, although their model slightly underestimates the bubble size at intermediate flow rates.

4.2. Bubble formation without liquid co-flow using the multi-needle gas sparger

Fig. 6b shows bubble diameters formed from the multi-needle sparger as a function of Q_n (bottom axis) and U_{sg}

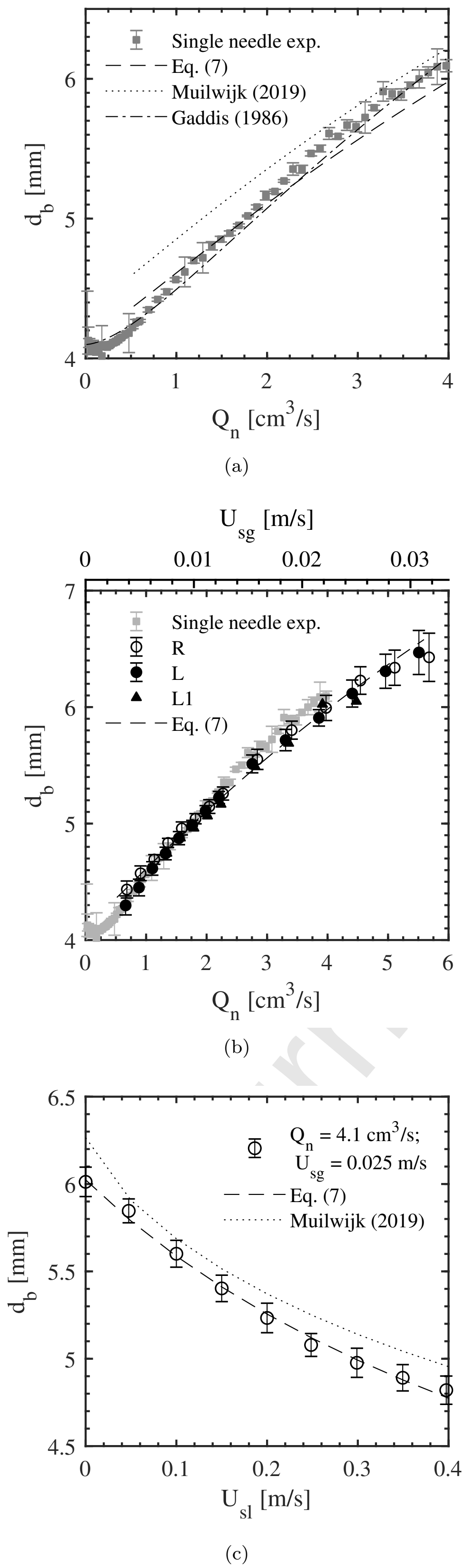

Figure 6: (a) Bubble diameter as a function of the needle gas flow rate for bubbles formed under constant flow conditions from a single submerged 1.55 mm i.d. needle. Results compared with the correlation found in Muilwijk and Van den Akker [25] (dotted line) for bubble formation under constant supply pressure. (b) Bubble diameters as a function of the gas flow rate per needle (bottom axis) and superficial gas velocity (top axis) for the multi-needle sparger. (c) Bubble diameter as function of the liquid co-flow velocity (U_{sl}) for a needle gas flow rate of 4.1 cm^3/s and U_{sg} = 0.025 m/s. Filled markers denote measurements taken on the left sparger (L); open markers denote measurements taken on the right sparger (R). Triangles show the measurements taken (on air chamber L1) with the microphone. The present model equation, Eq. (7), is given by the dashed lines.

(top axis). Q_n was varied in the range 0.75 - 5.7 cm^3/s (at gas sparger level pressure) and the resulting bubble diameter is in the range 4.5-7 mm. The left sparger (filled markers) and right sparger (open symbols) show almost identical behavior indicating a good similarity between the spargers of the left and right compartment.

For low gas flow rates, the diameter of bubbles formed from the multi-needle sparger (black markers) agree very well with those formed from a single submerged needle (grey squares). For higher gas flow rates, slightly larger bubbles were formed from the single submerged needle. Bubble-bubble interactions between the growing and departing bubble (Period-2 bubbling [49, 25]) may be different for bubble formation at a single submerged needle, whereas bubble-bubble interactions in the multi-needle sparger are governed by more complex mechanisms due to bubbles formed at neighboring needles.

The variation of bubble diameters of bubbles formed from the multi-needle sparger (with a common manifold for each group of 98 needles) is also slightly higher compared to bubbles formed from a single submerged needle. Small variations in the capillary diameters lead to variations in the individual nozzle flow rate with a variation in d_b as a result. Some needles stopped forming bubbles at $Q_n \approx 0.75$ cm^3/s and lower gas flow rates could not be measured without the occurrence of weeping in probably the most narrow capillaries (see Appendix A.1) which receive the lowest flow rates.

At gas flow rates above 6.5 cm^3/s (U_{sg} >0.03 m/s), the bubble formation rate could not be obtained as: (1) coalescence occurred at the nozzle and no single (separate) bubbles were formed and (2) large turbulent eddies in the liquid flow of the bubble column disturbed the bubble formation process and the uniform bubble size distribution is compromised.

The bubble diameters measured using a microphone connected to a pressurized chamber feeding multiple (98) needles (L1, black triangles) agree very well with the bubble diameters obtained from the high-speed camera (circles). The broadness of the peak in the spectrum of the microphone response signal (Fig. 5) may indicate the spreading in bubble formation rates (and bubble size distribution), but more experiments are required to quantify this effect. At higher flow rates Q_n, the peak becomes less distinct and eventually disappears as a result of the transition from the formation of single bubbles to coalescence occurring at the needle outlet.

4.3. Bubble formation with liquid co-flow using the multi-needle gas sparger

Fig. 6c shows the bubble diameter as function of liquid co-flow velocity. The gas flow per needle (corrected for the change in density) is fixed at a value of 4.1 cm^3/s (U_{sg} =0.025 m/s) and the liquid velocity is increased in steps of ≈ 0.05 m/s. Error bars are shown at ± one standard deviation from the mean value.

The bubble diameter decreases with increasing liquid co-flow velocity as a result of increasing drag force and bubble entrainment. Coalescence was not observed as the gas flow rate per nozzle is still within the regime for single bubble formation in the absence of co-flow. An increase of the liquid co-flow reduces interaction between the growing and departing bubble and transition to coalescence is delayed to higher gas flow rates. More experiments are required in order to find the transition to bubble formation with coalescence in the presence of liquid co-flow.

4.4. Discussion of a model equation for the bubble diameter

The model equation proposed in Ref. [25] was adjusted for bubble formation under constant flow condition and fitted to the data shown in Fig. 6b,c. We find that the bubble diameter can be very well described by:

$$\frac{d_b}{d_n} = \left[0.093\frac{U_l}{U_{g,n}} + \left(\left(\frac{6.18}{Bo}\right) + 1.26Fr^{3/5}\right)^{-1}\right]^{-\frac{1}{3}} \tag{7}$$

where,

$$Bo = \frac{\rho_w g d_n^2}{\sigma} \tag{8}$$

$$Fr = \frac{U_{g,n}^2}{g d_n} \tag{9}$$

$U_{g,n}$ is the linear needle gas velocity, $4Q_n/(\pi d_n^2)$, and U_l the liquid co-flow velocity and Bo = 0.32.

Due to the inserted capillaries imposing a constant flow condition in the present study, the above correlation differs from the correlation we found in our previous paper [25] when bubbles were formed under constant pressure conditions with weeping emerging at lower flow rates.

Eq. (7) is fitted for nozzle gas flow rates up to 5.7 cm^3/s and liquid co-flow velocities up to 0.4 m/s and plotted along with the data shown in Fig. 6 (dashed lines).

In case of no co-flow, coalescence starts occurring at a nozzle gas flow rate of ≈ 5.7 cm^3/s (U_{sg} ≈ 0.03 m/s), while the occurrence of coalescence is significantly delayed in the presence of co-flowing liquid due to the entrainment of preceding bubbles. Therefore, we expect Eq. (7) to work sufficiently well for higher gas flow rates with liquid co-flow.

Table 3: Overview of bed expansion experiments. BSD: bubble size distribution: (U)niform or (B)imodal. Measured chamber pressure P_{ch}: yes/no. The identifier in the most left column (series A-D) reflects which series were carried out with the same batch of water.

Series	H_0 [10^{-3} m]	β [m/(m/s)]	H_0/β [10^{-2}m/s]	BSD [U/B]	P_{ch} y/n
A1	808±1	4.42±0.04	18.3±0.2	U	y
A2	1277±1	6.57±0.05	19.4±0.1	U	y
A3	1274±1	6.62±0.04	19.2±0.1	B	y
B1	1605±1	8.47±0.06	19.0±0.1	U	y
C1	958±1	4.88±0.05	19.6±0.2	U	n
C2	1751±1	8.61±0.07	20.3±0.2	U	n
D	1427±1	7.00±0.04	20.4±0.1	U	n

More experiments may be required to test the validity of the model beyond the calibrated range and for different liquid properties (surfactants, water salinity).

It should be noted that, due to limited optical access to the needles in the center of the column, the nozzles at the outskirts of the grid were more accessible for visual inspection and results of the high-speed imaging may be biased towards the bubble formation rates at the column walls.

The position in the distributor/sparger (see Fig. 3) may influence the bubble formation rate due to a non-homogeneous pressure in the air chamber. In addition, as the Laplace pressure $4\sigma/d_n$ (≈ 1.8 mbar) is not negligible compared to the distributor pressure drop ΔP_d (≈ 2-50 mbar), the pressure in the air chamber may start to resonate with the bubble formation rate from the multi-needle sparger. At low flow rates, this may lead to slightly larger bubbles as compared to bubbles formed at strictly constant flow rate conditions.

It may be concluded that, considering the error sources described above, the gas spargers work very well and we are able to accomplish almost equal flow rate through all needles and to arrive at a uniform bubble size. The terminal bubble rise velocity for individual bubbles in the size range 4-7 mm is in the range 0.235-0.245 m/s, for both clean and contaminated water [29], as also given by the parametrized equation given by Park et al. [50]. Even when (for higher air flow rates) the actual bubble diameters deviate from the valued predicted by Eq. (7), their rise velocities may still be very similar.

5. Void fraction at uniform aeration

The overall gas fraction as a function of the superficial gas velocity (gas hold-up curve) is an important characteristic of a bubble column as the gas hold-up curve summarizes the complexity of the bubble column fluid dynamics [51]. The void fraction can be estimated by using the drift-flux model, where α depends on U_{sg}, U_{sl}, and the slip

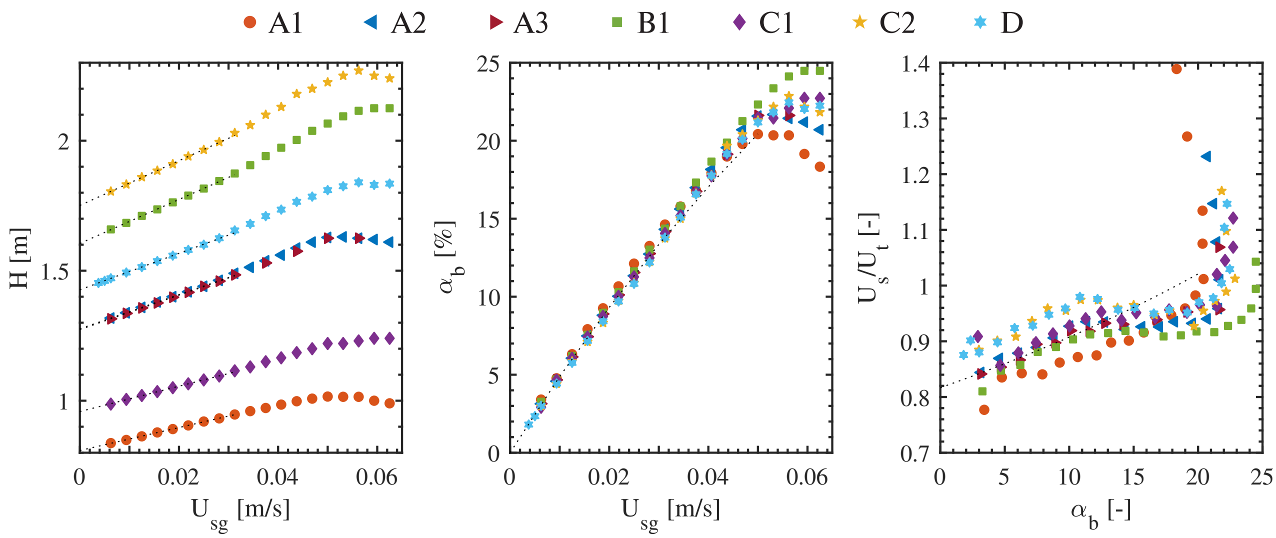

(a) (b) (c)

Figure 7: (a) Bed height, for various values of H_0, and (b) void fraction as function of superficial gas velocity. (c) Bubble swarm velocity divided by the bubble terminal rise velocity, see Eq. (11), as function of void fraction α_b.

velocity U_s:

$$U_g = \frac{U_{sg}}{\alpha} \tag{10a}$$

$$U_l = \frac{U_{sl}}{1-\alpha} \tag{10b}$$

$$U_s = U_g - U_l \tag{10c}$$

where U_g is the gas velocity and U_l the liquid velocity. The slip velocity U_s is a function of the terminal rise velocity of an isolated bubble U_t and a function of α to account for the presence of other bubbles:

$$U_s = U_t f(\alpha) \tag{11}$$

The overall gas fraction was obtained by two different methods, viz. bed expansion measurements and chamber pressure measurements (both discussed in Sec. 3), and the results are compared and discussed in this section. For the future, we plan to measure local void fractions, local bubble velocities and interfacial area data with the help of dual-tip optical fibre probes.

5.1. By bed expansion measurements

Fig. 7a shows bed height as function of superficial gas velocity for various values of H_0. We observe a linear increase in bed height for low gas velocities up to a critical gas velocity, after which a change in the slope of H occurs which corresponds to the transition of homogeneous to heterogeneous bubbly flow. The value of H_0, the liquid height at zero aeration, could not be measured directly as a superficial gas velocity of at least 0.004 m/s must be maintained to prevent weeping. An equation in the form of:

$$H = H_0 + \beta U_{sg} \tag{12}$$

was fitted to the homogeneous regime with a uniform bubble size distribution ($U_{sg} < 0.03$ m/s, see Sec. 4) to obtain H_0 (crossing of the dashed line and the y−axis) and the bed expansion coefficient β in m/(m/s) for each set of experiments. The coefficients of determination R^2 are >99.94 % for all series. The results are summarized in Tab. 3.

The overall gas hold up is then calculated using Eq. (2). Fig. 7b shows that the bed height curves collapse to a fairly similar curve when the void fraction Eq. (13) is plotted against the superficial gas velocity. The present results show that our bed expansion experiments are very repeatable and similar gas holdup curves were found for different values of H_0, performed with different batches of tap water. We did not find a significant influence of the aspect ratio, e.g. H_0, on the gas holdup curves.

A model equation for the void fraction follows from the observation of linear bed expansion at low superficial gas velocities. Combining Eq. (12) and Eq. (2) yields:

$$\alpha = \frac{U_{sg}}{H_0/\beta + U_{sg}} \tag{13}$$

and we find $H_0/\beta = 0.195 \pm 0.007$ m/s for the series shown in Tab. 3. We see that Eq. (13), dotted line, shows very good agreement with our data up to $U_{sg} = 0.03$ m/s and works reasonably well up to U_{sg} =0.05 m/s.

The slip velocity U_s is then calculated according to $U_s = U_{sg}/\alpha_b$, where α_b is the experimental data given in Fig. 7b. Fig. 7c shows U_s normalized by the (almost constant) terminal rise velocity U_t (=0.24 m/s) as a function of the void fraction α_b - see Eq. (11). We see that the non-dimensional slip velocity $f(\alpha)$ starts at a value in the range 0.78-0.9 and then increases to level off for void fractions in the range 10-15 %. Beyond α_b= 20%, we observe an increase in swarm velocities, which indicates the transition to a more heterogeneous regime for which Eq. (12) does not hold any longer. Large gradients in the bubble velocity were observed (fast rising in the centre, downward at the sides) and the drift-flux model is not valid in this regime.

Combining Eq. (10), (11) and (13), using U_{sl}=0, we find:

$$\frac{U_s}{U_t} = \frac{H_0/\beta}{U_t}\frac{1}{1-\alpha} \tag{14}$$

where $H_0/\beta \approx 0.82U_t$, which is given by the dotted line in Fig. 7c.

As many authors report a decreasing slip velocity with increasing α due to hindrance effects, $f(\alpha) < 1$ in Eq. (11), Simonnet et al. [39], McClure et al. [52] report that there is still no agreement on how to account for the drag force experienced by bubbles in a swarm. More experiments concerning local gas fractions, bubble velocities and liquid velocities are required to validate/develop a model for the drag correction factor for a bubble in a swarm as was attempted by McClure et al. [52].

We emphasize that our bubbles in the range 4-7 mm are very uniform in size, particularly for lower void fractions, very uniformly distributed and with an almost constant terminal velocity. This may result in a very calm and organized flow with virtually no bubbles pushing aside and passing each other. The reduction in mutual hindrance when increasing void fractions might be the result of an internal reshuffling of the bubble swarm structure.

5.2. By chamber pressure measurements

Void fractions can also be found by using Eq. (6) for which we need air chamber pressure measurements (see Appendix A.2) and measured liquid level heights H (as shown in Fig. 7a). These void fractions are denoted by α_p.

5.2.1. Without liquid co-flow

Fig. 8a shows a parity plot, where the void fraction α_p is compared with the void fraction obtained by bed expansion measurements α_b. We found that both methods agree very well for a large range of void fractions. Both methods may deviate from the actual void fraction. First, the bed expansion height can not be obtained with an accuracy of less than ± 2 mm (for low flow rates) and H_0 could not be determined without the approximation of linear bed expansion Eq. (12). Second, the plausibility of Eq. (6) is sensitive to the accuracy of the pressure sensors, the validity of ignoring the fluctuating Laplace pressure (due to growing and detaching bubbles), wall friction forces and the validity of Eq. (A.1) as gas compressibility may become important for higher values of H_0.

The bed expansion cannot be measured when the liquid surface rises as high as the column height, as the liquid loading H_0 will change due to the overflowing liquid. Fig. 8b shows the void fraction α_p as a function of superficial gas velocity as found from only chamber pressure

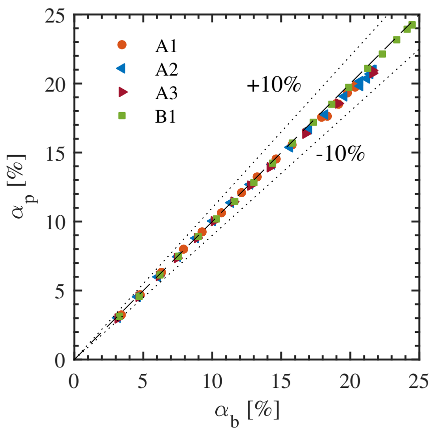

(a)

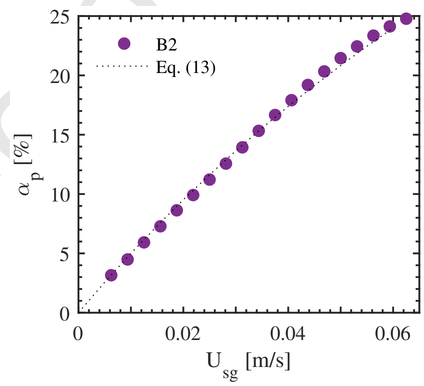

(b)

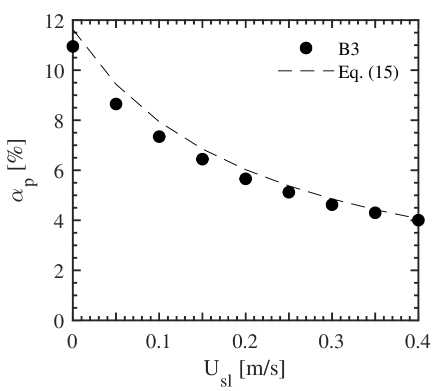

(c)

Figure 8: (a) Parity plot of the void fraction obtained by bed expansion measurements (Eq. (13), horizontal axis) and pressure measurements (Eq. (6), vertical axis) for a partially loaded column (H smaller than column height). See the legend in Fig. 7 for clarification of the symbols. Data only available when P_{ch} and H measured simultaneously (see Tab. 3). (b) Void fraction α_p, Eq. (6), as function of superficial gas velocity. Bed height is fixed as the column is filled up to the free surface. Eq. (13) is given by the dashed line, using H_0/β of series B1 (see Tab. 3). (c) Void fraction α_p, as function of superficial liquid velocity. The dashed line shows the calculated void fraction by the drift-flux model. U_{sg} =0.025 m/s.

measurements in series B2 (see Fig. A.14a) when water height equals column height and bed expansion could not be measured. The void fraction as a function of U_{sg} for a fully loaded column (fixed H, free overflow at the top of the column) is very well described by our Eq. (13) up to U_{sg}=0.05 m/s.

5.2.2. With liquid co-flow

In case of liquid co-flow, bed bed expansion measurements cannot be performed either. Fig. 8c shows the measured void fraction, again from chamber pressure measurements only (series B3, see Fig. A.14b), as a function of superficial liquid velocity while the superficial gas velocity was kept constant at a value of 0.025 m/s. We assumed that the discharge height (the excess height above the column height due to the overflowing liquid), linearly increased up to 4 cm at a superficial liquid velocity of 0.4 m/s. The void fraction α_p (black bullets) are calculated using this discharge height correction for H.

The void fraction is calculated using Eq. (10) and Eq. (14), which yields:

$$\alpha = \frac{U_{sg}}{U_{sg} + U_{sl} + H_0/\beta} \tag{15}$$

The model prediction for the void fraction in the presence of liquid co-flow is shown as a dashed line in Fig. 8c and agrees very well with the measured void fraction. However, more experiments with different methods (e.g. optical bubble probes) are required to validate the model as the chamber pressure sensors may not be sufficiently sensitive and accurate to measure small pressure differences to resolve low void fractions. Also, the crude approximation made for the discharge height to correct H has a significant effect on the void fraction derived using Eq. (6), as a change of 4 cm water in hydrostatic pressure results in a difference of ≈ 1% in the calculated void fraction.

5.3. Literature comparison

An extensive overview of gas hold-up measurements is given by Gandhi and Joshi [53]. A very large spread in the measured void fractions as function of U_{sg} was found by different researchers, resulting in many different empirical correlations to describe the void fraction as function of superficial gas and liquid velocities, column geometries, gas sparger types and fluid properties.

Fig. 9 shows a comparison of our proposed correlation for the overall gas holdup (dashed line) with a selection of some relevant reported gas holdup curves. The inserted figure shows a close up for U_{sg} up to 0.025 m/s.

The influence of the sparger type on the gas hold-up is clearly illustrated by the studies of Mudde et al. [31], Drahoš et al. [30], Groen et al. [18], Besagni et al. [43], Sharaf et al. [32], Pjontek et al. [34]. Fine spargers (needle spargers, perforated plate with small hole diameters), producing small and uniform bubbles, stabilize the homogeneous bubbly flow regime with a high gas hold-up as a result. Coarse spargers (spider spargers, perforated plate with large hole diameters) produce a much lower gas hold-up due to (1) the initially poor homogeneous distribution of bubbles and/or (2) the formation of a non-uniform primary distribution of bubble sizes, leading to rapid breakup and coalescence of bubbles and an advanced transition to turbulent bubbly flow (with coherent vortical structures in the liquid phase).

The column diameter (see Groen et al. [18], porous plate sparger) is found to have a negligible effect on the gas hold-up.

Mudde et al. [31], Sharaf et al. [32] also report on the water type used. Mudde et al. [31] showed that a transition to turbulent bubbly flow was observed at a gas hold-up of 35% when fresh tap water (3 hours old) was used, whereas a gas hold-up of 55 % could be obtained in the homogeneous regime when aged tap water (3 weeks old) was used. For both cases, the increased gas hold-up is due to lower bubble rise velocities in contaminated water, although, this effect is minimal when a coarse sparger is used (see data of Sharaf et al. [32]).

In the study of Lau et al. [33], no significant difference was found for different values for the unaerated liquid height. The lower gas hold-up values may be a result of the confined bubble column dimensions leading to faster bubble rise velocities and a lower gas hold-up.

We find very good agreement of our results (dashed line) with the studies of Alméras et al. [17], Van Gils [42] (needle spargers, d_b = 3 mm) and Besagni et al. [43] (perforated plate sparger). For higher U_{sg}, we find lower gas hold-ups than Mudde et al. [31] (3.5< d_b <5.0 mm), which may be due to the larger, faster rising bubbles in the present study (4.5< d_b <7 mm).

It should be noted that void fractions measured using an optical probe (Ref. [39, 34, 17, 31, 18]) may underestimate the gas fraction, especially for small bubbles at low U_{sg}. This may explain some irregularities in the reported gas hold-up curves.

While overall our void fraction data fall amidst all data reported by many authors, an attractive feature of our data is that they have been obtained with bubbles in the range 4-7 mm which are very uniform in size, particularly for lower void fractions, very uniformly distributed and with an almost constant terminal velocity. This turns our data very suitable for validating Euler-Euler simulations performed for a single bubble size as input parameter.

6. Non-uniform aeration cases

6.1. Formation of a bi-modal size distribution

For the formation of a bi-disperse bubble size mixture, the distribution of gas flow between a set of chambers (R1/R2 and L1/L2) was altered by adjusting the split ratio X (see Fig. 1). Partially closing the gate valves for the air supply lines of chamber R1 and L1 results in less

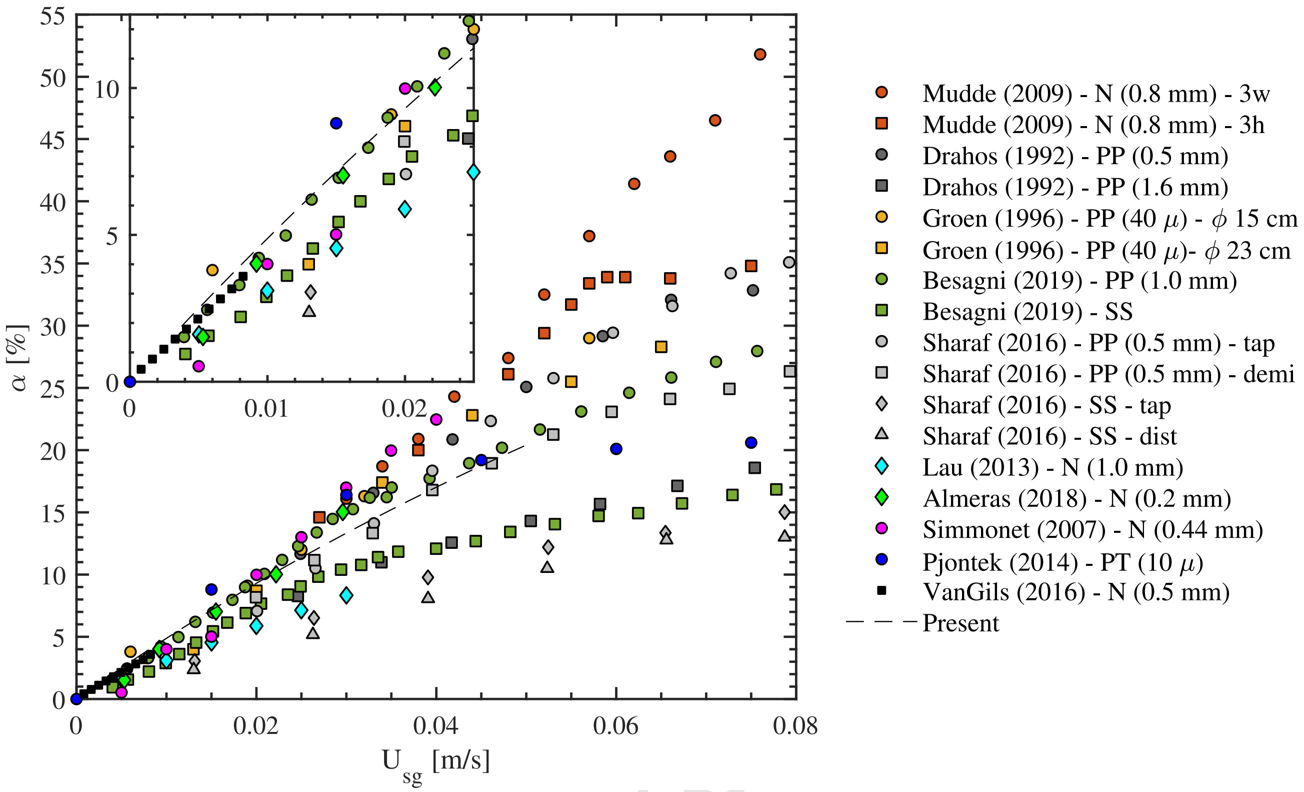

Figure 9: Comparison of gas holdup curves with previously reported data. PP: Porous plate; PT: Porous tube; SS: Spider sparger; N: Needle sparger.

flow to chamber R1 and L1 and more flow to chambers R2 and L2, hence a lower chamber pressure for chamber R1, L1 and a higher chamber pressure for chamber R2,L2 (see also series A3 in Fig. A.14a) and we derived the split ratio from the rotameter readings. The values of X are limited by the lowest possible flow rate of ≈ 5 L/min per chamber ($Q_n \approx 0.75$ cm^3/s) to prevent weeping and water entering the air chambers.

Bi-modal bubble formation rates (see Fig. 10a,c) were measured corresponding to bubbles formed from chambers R2, L2 (higher chamber flow rate) and chamber R1,L1 (lower chamber flow rate), while operating at a split ratio of $X \approx 38$ %. Figs. 10b,d show the resulting bubble diameter as calculated using Eq. (1). At low gas flow rates (top row), a clear bi-modality was observed in the bubble formation rates with a slight bi-modality in d_b as a result. At high gas flow rates (bottom row) bubbles from both chambers (R1, R2) were formed at an almost similar formation rate, while a clear bimodal bubble size distribution was obtained due to the differences in Q_n for chamber R1 and R2.

Fig. 11 shows the bubble diameters as function of superficial gas velocity. We are able to create a mixture of bubbles with a sharp bimodal size distribution. The larger bubbles are formed from chambers L2, R2 (receiving more gas flow rate) and the smaller bubbles are formed from chamber L1, L2 (receiving less gas flow rate). Bubbles formed from air chamber R2 and L2 are in the range 4.7-6.6 mm, whereas bubbles formed from chamber R1 and L1 are in the range 4.6-5.7 mm. The somewhat larger spreading in the calculated bubble diameter at low flow rates is due to the propagation of inaccuracy in rotameter readings (to calculate X and Q_n) as the bubble formation rate distributions were found to be very narrow.

At high needle gas flow rates, the bubble diameter is a function of gas flow rate, whereas at low gas flow rates, (in the quasi-static flow regime) bubbles detach with a critical constant diameter (see also Fig. 6a). Therefore, bubble diameters from R1 vs. R2 and from L1 vs. L2 hardly differ at low flow rates. Thus, applying a split ratio in the surface tension controlled regime will only alter the bubble formation rate and not the resulting bubble diameter.

The ratio of the bubble size from R2/L2 to the bubble size from R1/L1 is 1.15 maximum. Note that in the pertinent bubble size range all bubbles move more or less with the same velocity, i.e. bubble speed is irrespective of bubble size [29]. This may explain why in Fig. 7 the aerated liquid heights for Series A2 and A3 are almost identical and the volume fractions for these Series in Fig. 8a also coincide.

Eq. (7) can be used to predict bi-modalities for other operating conditions $(X, U_{sg,s}, U_{sl,s})$. While the bi-modality

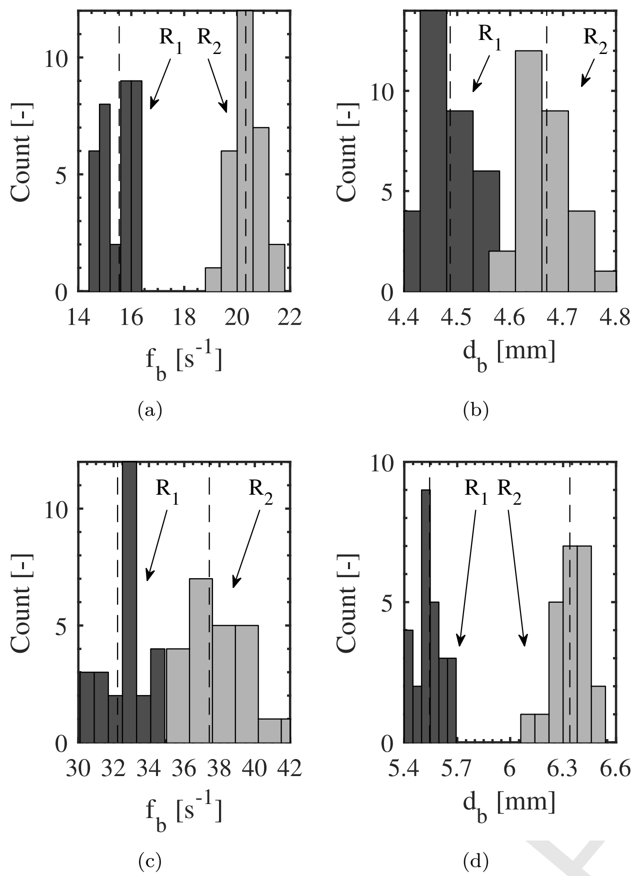

Figure 10: Histograms of the bubble formation rates (left) and bubble diameters at gas sparger level (right) at unequal gas distribution between a pair of chambers R1/R2. Top: U_{sg} =0.005 m/s; bottom: U_{sg} =0.022 m/s. $X \approx 38\%$.

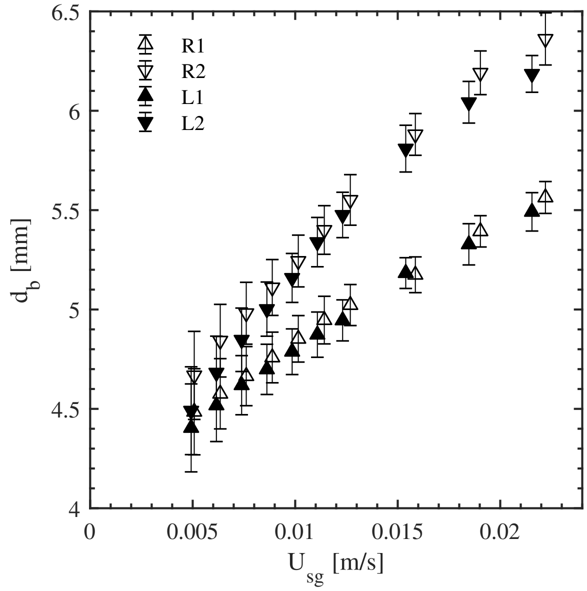

(a)

Figure 11: Bubble diameters for bubbles formed at unequal gas distribution between a pair of chambers as function of the superficial gas velocity U_{sg}. $Q_{L1}/Q_{L2} \approx Q_{R1}/Q_{R2} \approx 0.6$, hence, $X \approx 38\%$. A bi-modal bubble formation rate/bubble size distribution was found and the mean (symbol) and standard deviation (error bars) are shown for both modes. The flow rates per needle are calculated using the individual chamber flow rates divided by 98 needles.

is subtle (no difference in bed expansion characteristics was found for the case of a bi-modal size distribution, see series A2, A3 in Fig. 7) in the absence of co-flowing liquid, a different sparger design (different nozzle diameter for each chamber) would be needed to obtain bubbles with a larger difference in bubble size.

6.2. Mixing patterns at unequal aeration

The column was filled with an amount of water such that H_0 = 113 cm. Images of the flow channel were captured on a Sony IMX258 (3.59 mm lens) at a resolution of 540 × 960 pix at a frame rate of 120 Hz for various settings of the gas flow rates on the left and right side of the column, while the column was illuminated by a 20W continuous LED light. Images, slightly contrast enhanced and sharpened, are averaged over a period of 0.2 s (24 images) to obtain bubble streaks. Videos of the embedded images can be found in the Supplementary Material.

Fig. 12 shows the obtained bubble streaks for four different settings of the gas flow rates. The difference in superficial gas fraction is increasing from the left to the right.

Equal gas flow rates were supplied to both sides in Fig. 12a, where we found that the bubbles on the left side of the column seem to move slightly faster. A correction of ±1.5 % of the setpoint for both mass flow controllers was sufficient to balance the superficial gas velocities of the left and right side of the column and the velocity profile in Fig. 12b appears to be symmetric.

Applying a factor 1.5 and 2.5 difference in the superficial gas velocities left and right (left higher) results in a very different flow behavior as shown by the bubble streaks in Fig. 12c,d respectively. In both cases, the higher gas flow rate left entrains liquid and bubbles from the right, creating a buoyancy driven upward flow with a large vortex and with bubbles moving downward at the far right side as a result.

Currently, we are developing a type of bubble image velocimetry technique correlating high-resolution images of larger sections of the column to study flow patters including vortical flow structures.

7. Conclusions

A new bubbly flow test rig (“LimBuRig”) was built with the view of collecting accurate experimental under precisely documented conditions for the purpose of validating Euler-Euler CFD simulations of bubbly flows. The

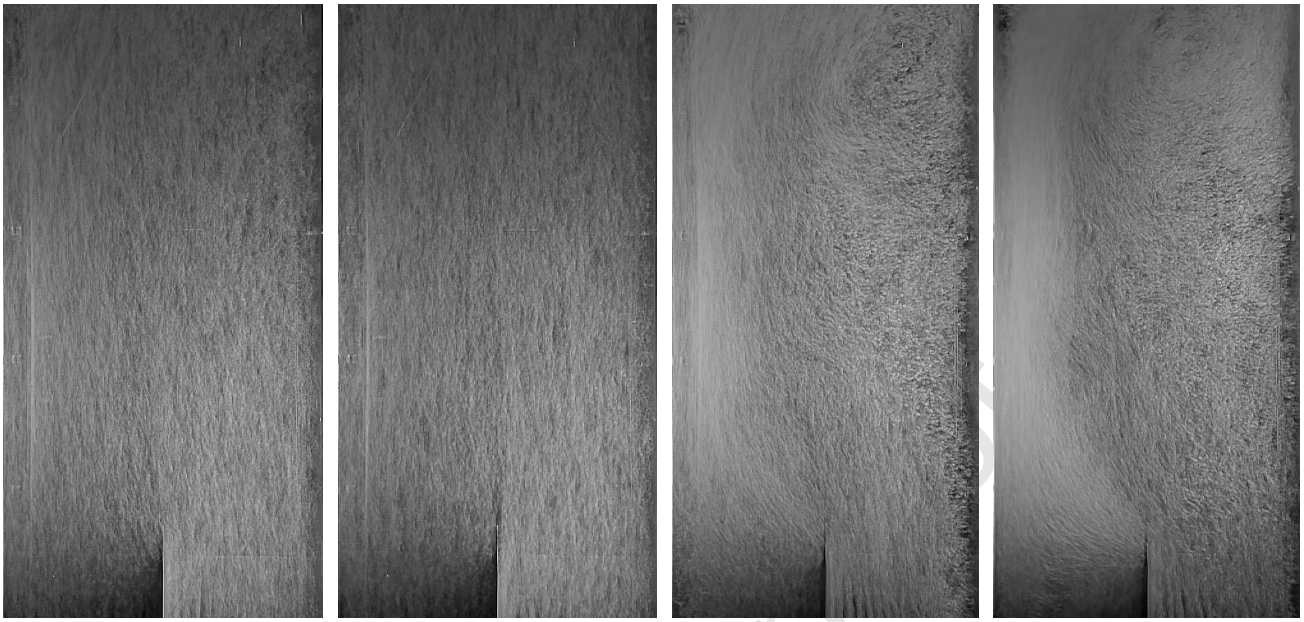

(a) U_{sg} =0.625-0.625 cm/s (b) U_{sg} =0.606-0.644 cm/s (c) U_{sg} =0.938-0.625 cm/s (d) U_{sg} =1.563-0.625 cm/s

Figure 12: Bubble streaks for four different gas flow rate settings. The numbers are the superficial gas velocity for the left and right side of the column respectively. Bubble streaks are obtained by averaging a series of 24 images (0.2 s @ 120 Hz). Illumination is from the right, giving some shadow in the lower left part.

rectangular column consists of two square sections, each with its own gas and liquid supply and the bubbles being produced from 4×98 needles, evenly distributed across the bottom of these two square sections. The column is able to

- operate with and without liquid co-flow;
- produce bubbles of an almost uniform size in the range 4-7 mm which all rise with the same terminal velocity [29];
- produce bubbles with an essentially bi-modal size distribution within the range 4-7 mm, the ratio of the two mean bubble diameters being maximum 1.15;
- create a very uniformly aerated bubbly flow in the entire column for varying water heights;
- create two separate bubbly flows, from the two square sections, with different gas and liquid flow rates and with the same or different bubble sizes, with the view of studying their interaction and mixing,

To get all needles bubbling and bubbling at the same formation rate, we had to insert additional restrictions in the supply lines to the needles, with the view of creating extra pressure drop. As a result, the correlation for dimensionless bubble size as a function of Bond and Froude numbers had to be modified slightly (compared to the single needle data reported previously [25]). Bubble formation rates were measured by both high-speed imaging and a simple acoustical method. The clear peaks in the acoustic spectra coincide with the bubbling rates found by image analysis. This confirms our previous conclusion [25] that using a (low cost) microphone is an elegant way of measuring bubble formation rates.

Overall volume fractions in the column were determined by means of bed expansion as well as air chamber pressure measurements. While the two methods gave very similar results, the latter is also applicable when bed expansion cannot be measured in the case of e.g. liquid co-flow. In the absence of liquid co-flow, we were able to create a homogeneous bubbly flow up to an overall gas volume fraction of ≈ 20 %. We found overall volume fraction without liquid co-flow to increase almost linearly with increasing air flow rate over a substantial range of gas flow rates, while at a specific air flow rate it decreased in a nonlinear way with increasing liquid flow rate. We found slip velocity to increase with increasing void fraction.

In a series producing bi-modal bubble size distributions in the range 4-7 mm, the ratio of the two bubble sizes was 1.15 maximum. We hardly found a difference in overall bubbling performance as a result of such bi-modal distributions. Finally, we presented visual observations of overall flow patterns in the case of unequal aeration of the left and right parts of the column, for the time being in the absence of liquid co-flow.

Ackowledgements

This research was made possible through a start-up fund in the context of the Bernal Project at the University of Limerick.

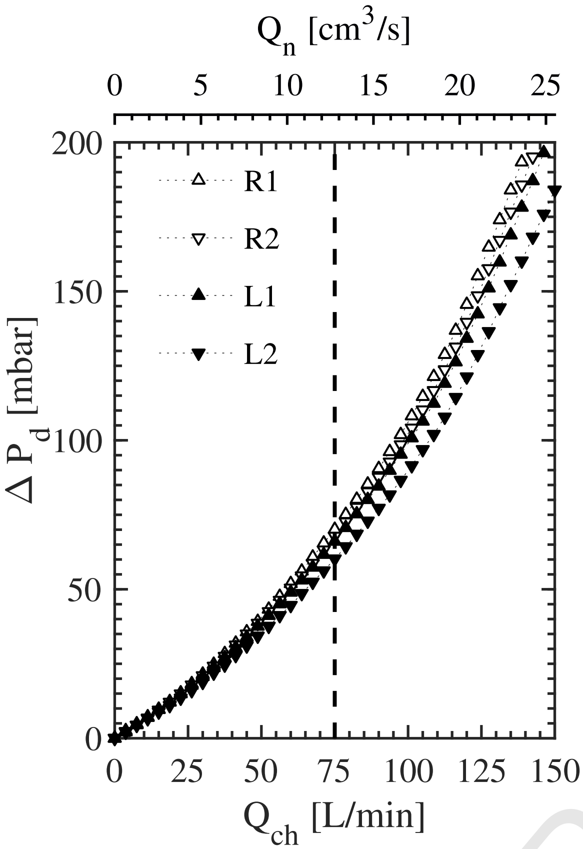

Figure A.13: Measured distributor pressure drops as function of gas flow rate per chamber for the four chambers. The variation between the four chambers is due to the grouping of the capillaries by their orifice constant. Under normal operation (equal gas supply to all chambers, X=50%), the flow rate per chamber Q_{ch} ranges up to 75 L/min (vertical dashed line) at a maximum superficial gas velocity U_{sg} = 0.0625 m/s.

Appendix A. Chamber pressure measurements

Appendix A.1. Pressure measurements for Eq. (3)

Table A.4: Fitting coefficients in Eq. A.1.

Chamber Q_{ch}	$10^{-3}a$ $\left[\frac{\text{mbar}}{(\text{L/min})^2}\right]$	$10^{-3}b$ $\left[\frac{\text{mbar}}{\text{L/min}}\right]$	c [mbar]
< 75 L/min			
R1	4.89±0.03	570±2	
R2	4.49±0.05	569±3	
L1	4.19±0.06	566±3	
L2	3.82±0.05	517±3	
> 75 L/min			
R1	13.2±0.4	-875±57	61.9±2.4
R2	12.4±0.3	-815±56	59.1±2.4
L1	11.6±0.3	-734±46	55.8±2.0
L2	9.70±0.24	-518±40	44.5±1.8

In order to minimize the variation in pressure drop characteristics between the 98 outlets of a distributor, the 392 (4×98) capillaries, see Sec. 2.2.2, were sorted in four categories according their orifice constant $Q_i/\Delta P_i$, i=1..392. A gas flow rate was fixed at 11.6 cm^3/s and the capillaries were sorted in groups of 98 by their pressure drop in the following categories: 46-48, 52-54, 54-56 and 56-58 mbar, which are installed in the chambers L2, L1, R2, R1 respectively. In this way, the gas distribution from a chamber to its outlets is optimized. As a result, each distributor has a slightly different pressure drop characteristic.

Fig. A.13 plots the pressure drop across the distributor $\Delta P_{d,ch}$ as a function of the gas flow rate through an air chamber Q_{ch}, while the needle outlets were at atmospheric pressure (empty column). The distributor pressure drop (capillary + flexible tube + needle) for each chamber can be very well approximated by a combination of a laminar ~ Q_{ch} and turbulent ~ Q_{ch}^2 contribution to the pressure drop:

$$\Delta P_{d,ch} = a_{ch}Q_{ch}^2 + b_{ch}Q_{ch} + c_{ch} \tag{A.1}$$

A second order polynomial, Eq. (A.1), was fitted for the chamber pressures for chamber flow rates in the range of 0-75 L/min (capillary Re < 2000) for normal operation (all pressurized chambers equally used) and c_{ch} was forced to 0. In case one of the chambers is set to a reduced flow rate, the other chamber receives a higher flow rate, possibly beyond 75 L/min, for which a polynomial is fitted with $c_{ch} \neq 0$.

The values of a_{ch}, b_{ch} and c_{ch}, given in Tab. A.4, are obtained by minimization of the square residuals and the coefficient of determination (R^2) is 99.98% or higher for all four chambers. Eqs. (A.1), for each chamber ch, also serve as a reference for proper functioning of the distributors, where deviant pressure drops characteristics will be found when needles are blocked (in case of weeping).

Appendix A.2. Chamber pressure measurements to determine the void fraction using Eq. (6)

Fig. A.14a shows recorded chamber pressures, for the four chambers (L1,L2,R1,R2), as function of the gas flow rate (bottom axis) and superficial gas velocity (top axis) without liquid co-flow (series A1-A3, B1-B2).

For the series A1, A2, B1, the chamber pressures increase quadratically with increasing gas flow rates due to the pressure drops over the distributors and for these series, $P_{R1} > P_{R2} > P_{L1} > P_{L2}$ which is in accordance with the distributor pressure drop curves shown in Fig. A.13.

For series A3, a split ratio X of ≈ 38 % was applied and the air chambers L2, R2 show a higher pressure than L1, R1, which indicate higher flow rates to L2, R2, than to chamber L1, R1 (to create a bi-disperse bubble size distribution).

The needle outlet pressure, Eq. (3), see dashed lines Fig. A.14a, is constant for each of the series A1-A3 and B1, which confirms that H_0 is independent of U_{sg}. The difference in P_{no} between series A1, A2, and B1 is due to the difference in unaerated liquid level height H_0.

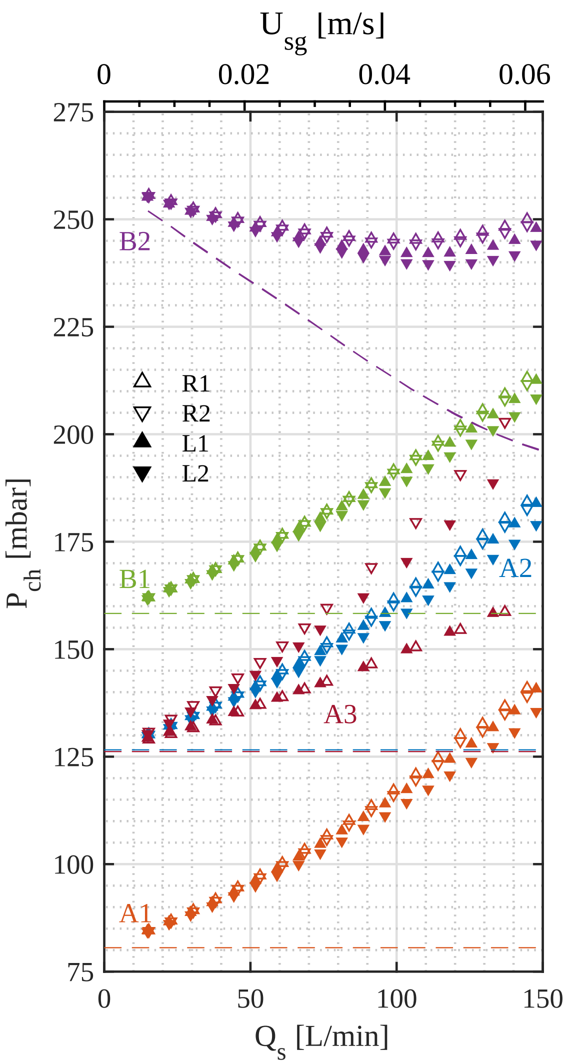

(a)

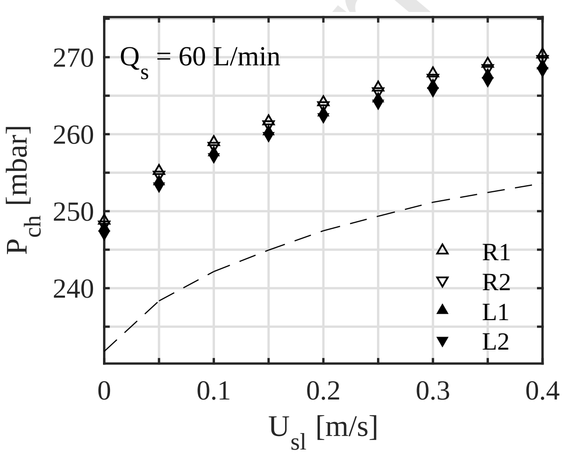

(b)

Figure A.14: Chamber pressures as function of (a) the gas flow rate per compartment ($Q_s = Q_L = Q_R$) in the absence of liquid co-flow and (b) as a function of the superficial liquid velocity U_{sl} for Q_s = 60 L/min (U_{sg} = 0.025 m/s). The dashed lines show the needle outlet pressure P_{no} as given by Eq. (3). The colors refer to the series A1-A3,B1-3 as in Fig. 7 and/or Fig. 8a,b,c.

Chamber pressures obtained with a fully loaded column (H equals column height) are given by series B2 in Fig. A.14a. At low gas flow rates, chamber pressures decrease with increasing gas flow rate due to the increasing void fraction (and decreasing $H(1-\alpha)$), while at higher flow rates, chamber pressures increase again as distributor pressure drops $\Delta P_{d,ch}$ increase quadratically with the gas flow rate. The needle outlet pressure P_{no} decreases monotonically with increasing gas flow rate, indicating a monotonic increase of the void fraction (decrease of liquid head due to the overflowing liquid).

Fig. A.14b shows recorded chamber pressures as a function of the superficial liquid velocity U_{sl}. Q_s was set at 60 L/min ($U_{sg} = 0.025$ m/s) and U_{sl} was in the range 0-0.4 m/s. As the gas flow rate was kept constant, the distributor pressure drop ΔP_d was constant.

Both the chamber pressures (symbols) and the needle outlet pressure (Eq. (3, dashed line) increases with increasing co-flow velocity, resulting in a higher hydrostatic pressure and a lower void fraction for increasing U_{sl}.

References

[1] D. F. Fletcher, D. D. McClure, J. M. Kavanagh, G. W. Barton, CFD simulation of industrial bubble columns: Numerical challenges and model validation successes, Applied Mathematical Modelling 44 (2017) 25 – 42.

[2] H. E. A. Van den Akker, The euler-euler approach to dispersed two-phase flows in the turbulent regime, ERCOFTAC Bulletin 36 (1998) 30–33.

[3] M. Pourtousi, J. N. Sahu, P. Ganesan, Effect of interfacial forces and turbulence models on predicting flow pattern inside the bubble column, Chemical Engineering and Processing: Process Intensification 75 (2014) 38–47.

[4] S. Lo, Application of the MUSIG model to bubbly flows., AEA Technology (1996).

[5] D. Lucas, E. Krepper, H.-M. Prasser, Prediction of radial gas profiles in vertical pipe flow on the basis of bubble size distribution, International Journal of Thermal Sciences 40 (2001) 217 – 225.

[6] A. Vaidheeswaran, T. Hibiki, Bubble-induced turbulence modeling for vertical bubbly flows, International Journal of Heat and Mass Transfer 115 (2017) 741–752.

[7] H. Zhang, T. Yokomine, T. Kunugi, Turbulence modulation of the upward turbulent bubbly flow in vertical ducts, Nuclear Engineering and Technology 47 (2015) 513–522.

[8] Z. Khan, V. H. Bhusare, J. B. Joshi, Comparison of turbulence models for bubble column reactors, Chemical Engineering Science 164 (2017) 34–52.

[9] R. Rzehak, E. Krepper, CFD modeling of bubble-induced turbulence, International Journal of Multiphase Flow 55 (2013) 138–155.

[10] R. Rzehak, E. Krepper, Bubble-induced turbulence: Comparison of CFD models, Nuclear Engineering and Design 258 (2013) 57 – 65.

[11] R. Rzehak, S. Kriebitzsch, Multiphase CFD-simulation of bubbly pipe flow: A code comparison, International Journal of Multiphase Flow 68 (2015) 135–152.

[12] R. Rzehak, M. Krauß, P. Kováts, K. Zähringer, Fluid dynamics in a bubble column: New experiments and simulations, International Journal of Multiphase Flow 89 (2017) 299–312.

[13] R. M. Masood, A. Delgado, Numerical investigation of the interphase forces and turbulence closure in 3D square bubble columns, Chemical Engineering Science 108 (2014) 154–168.

[14] M. T. Dhotre, N. G. Deen, B. Niceno, Z. Khan, J. B. Joshi, Large eddy simulation for dispersed bubbly flows: A review,

International Journal of Chemical Engineering 2013 (2013) 1–22.

[15] D. D. McClure, H. Norris, J. M. Kavanagh, D. F. Fletcher, G. W. Barton, Validation of a Computationally Efficient Computational Fluid Dynamics (CFD) Model for Industrial Bubble Column Bioreactors, Industrial & Engineering Chemistry Research 53 (2014) 14526–14543.

[16] G. Besagni, F. Inzoli, T. Ziegenhein, D. Lucas, Computational fluid-dynamic modeling of the pseudo-homogeneous flow regime in large-scale bubble columns, Chemical Engineering Science 160 (2017) 144 – 160.

[17] E. Alméras, C. Plais, V. Roig, F. Risso, F. Augier, Mixing mechanisms in a low-sheared inhomogeneous bubble column, Chemical Engineering Science 186 (2018) 52–61.

[18] J. S. Groen, R. G. C. Oldeman, R. F. Mudde, H. E. A. van den Akker, Coherent structures and axial dispersion in bubble column reactors, Chemical Engineering Science 51 (1996) 2511–2520.

[19] R. C. Chen, J. Reese, L. S. Fan, Flow structure in a three-dimensional bubble column and three-phase fluidized bed, AIChE Journal 40 (1994) 1093–1104.

[20] K. J. Sene, J. C. R. Hunt, N. H. Thomas, The role of coherent structures in bubble transport by turbulent shear flows, Journal of Fluid Mechanics 259 (1994) 219.

[21] V. Roig, C. Suzanne, L. Masbernat, Experimental investigation of a turbulent bubbly mixing layer, International Journal of Multiphase Flow 24 (1998) 35–54.

[22] E. Climent, J. Magnaudet, Dynamics of a two-dimensional upflowing mixing layer seeded with bubbles: Bubble dispersion and effect of two-way coupling, Physics of Fluids 18 (2006) 103304.

[23] H. Ayed, J. Chahed, V. Roig, Hydrodynamics and mass transfer in a turbulent buoyant bubbly shear layer, AIChE J. 53 (2007) 2742–2753.

[24] A. L. De Tournemine, V. Roig, Self-excited oscillations in buoyant confined bubbly mixing layers, Physics of Fluids 22 (2010) 023301.

[25] C. Muilwijk, H. E. A. Van den Akker, Experimental investigation on the bubble formation from needles with and without liquid co-flow, Chemical Engineering Science 202 (2019) 318 – 335.

[26] R. E. Poorte, A. Biesheuvel, Experiments on the motion of gas bubbles in turbulence generated by an active grid, Journal of Fluid Mechanics 461 (2002) 127–154.

[27] M. Lance, J. Bataille, Turbulence in the liquid phase of a uniform bubbly air-water flow, Journal of Fluid Mechanics 222 (1991) 95–118.

[28] W. K. Harteveld, R. F. Mudde, H. E. A. Van Den Akker, Dynamics of a Bubble Column: Influence of Gas Distribution on Coherent Structures, The Canadian Journal of Chemical Engineering 81 (2003) 389–394.

[29] R. Clift, J. Grace, M. Weber, M. Weber, Bubbles, Drops, and Particles, Academic Press, 1978.

[30] J. Drahoš, J. Zahradník, M. Fialová, F. Bradka, Identification and modelling of liquid flow structures in bubble column reactors, Chemical Engineering Science 47 (1992) 3313 – 3320.

[31] R. F. Mudde, W. K. Harteveld, H. E. A. van den Akker, Uniform Flow in Bubble Columns, Industrial & Engineering Chemistry Research 48 (2009) 148–158.

[32] S. Sharaf, M. Zednikova, M. C. Ruzicka, B. J. Azzopardi, Global and local hydrodynamics of bubble columns – effect of gas distributor, Chemical Engineering Journal 288 (2016) 489 – 504.

[33] Y. Lau, K. T. Sujatha, M. Gaeini, N. Deen, J. Kuipers, Experimental study of the bubble size distribution in a pseudo-2d bubble column, Chemical Engineering Science 98 (2013) 203 – 211.

[34] D. Pjontek, V. Parisien, A. Macchi, Bubble characteristics measured using a monofibre optical probe in a bubble column and freeboard region under high gas holdup conditions, Chemical Engineering Science 111 (2014) 153 – 169.

[35] F. Magaud, M. Souhar, G. Wild, N. Boisson, Experimental study of bubble column hydrodynamics, Chemical Engineering Science 56 (2001) 4597 – 4607.

[36] E. Krepper, B. N. R. Vanga, A. Zaruba, H.-M. Prasser, M. A. L. de Bertodano, Experimental and numerical studies of void fraction distribution in rectangular bubble columns, Nuclear Engineering and Design 237 (2007) 399 – 408.

[37] R. Lau, R. Mo, W. S. B. Sim, Bubble characteristics in shallow bubble column reactors, Chemical Engineering Research and Design 88 (2010) 197 – 203.

[38] W. T. Medjiade, A. R. Alvaro, A. Schumpe, Flow regime transitions in a bubble column, Chemical Engineering Science 170 (2017) 263 – 269. 13th International Conference on Gas-Liquid and Gas-Liquid-Solid Reactor Engineering.

[39] M. Simonnet, C. Gentric, E. Olmos, N. Midoux, Experimental determination of the drag coefficient in a swarm of bubbles, Chemical Engineering Science 62 (2007) 858 – 866.

[40] H. Letzel, J. Schouten, R. Krishna, C. van den Bleek, Gas holdup and mass transfer in bubble column reactors operated at elevated pressure, Chemical Engineering Science 54 (1999) 2237 – 2246.

[41] B. Thorat, A. Shevade, K. Bhilegaonkar, R. Aglawe, U. P. Veera, S. Thakre, A. Pandit, S. Sawant, J. Joshi, Effect of sparger design and height to diameter ratio on fractional gas hold-up in bubble columns, Chemical Engineering Research and Design 76 (1998) 823 – 834. Particle Technology.

[42] D. Van Gils, Twente University of Technology, personal communication, 2016.

[43] G. Besagni, L. Gallazzini, F. Inzoli, On the scale-up criteria for bubble columns, Petroleum 5 (2019) 114 – 122. SI: Experimental & Numerical Study of Multiphase Flow Phenomena and Models in Oil & Gas Industry.

[44] B. K. Rana, A. K. Das, P. K. Das, Study of interaction pattern between bubbles at three inline orifices in a submerged pool, Chemical Engineering Science 168 (2017) 41–54.

[45] B. K. Rana, A. K. Das, P. K. Das, Towards the understanding of bubble-bubble interaction upon formation at submerged orifices: A numerical approach, Chemical Engineering Science 161 (2017) 316 – 328.

[46] S. Nedeltchev, U. Hampel, M. Schubert, Experimental study on the radial distribution of the main transition velocities in bubble columns, WIT Transactions on Engineering Science 89 (2015) 127–138.

[47] H. N. Oguz, A. Prosperetti, Dynamics of bubble growth and detachment from a needle, Journal of Fluid Mechanics 257 (1993) 111 – 145.

[48] E. S. Gaddis, A. Vogelpohl, Bubble Formation in quiescent liquids under constant flow conditions, Chemical Engineering Science 41 (1986) 97–105.

[49] V. V. Buwa, D. Gerlach, F. Durst, E. Schlücker, Numerical simulations of bubble formation on submerged orifices: Period-1 and period-2 bubbling regimes, Chemical Engineering Science 62 (2007) 7119 – 7132. 8th International Conference on Gas-Liquid and Gas-Liquid-Solid Reactor Engineering.

[50] S. H. Park, C. Park, J. Lee, B. Lee, A simple parameterization for the rising velocity of bubbles in a liquid pool, Nuclear Engineering and Technology 49 (2017) 692 – 699.

[51] G. Besagni, F. Inzoli, T. Ziegenhein, Two-Phase Bubble Columns: A Comprehensive Review, ChemEngineering 2 (2018) 13.

[52] D. D. McClure, J. M. Kavanagh, D. F. Fletcher, G. W. Barton, Experimental investigation into the drag volume fraction correction term for gas-liquid bubbly flows, Chemical Engineering Science 170 (2017) 91 – 97. 13th International Conference on Gas-Liquid and Gas-Liquid-Solid Reactor Engineering.

[53] A. B. Gandhi, J. B. Joshi, Unified correlation for overall gas hold-up in bubble column reactors for various gas–liquid systems using hybrid genetic algorithm-support vector regression technique, The Canadian Journal of Chemical Engineering 88 (2010) 758–776.

Newly designed bubbly flow rig with liquid co-flow for experimental validation of CFD

Precise needle sparger for creating a mono- or bi-disperse bubble size distribution

A new correlation for overall gas hold-up in a rectangular (40 x 20 cm) bubble column

Unequal lateral distribution of gas/liquid to study (buoyancy driven) mixing patterns

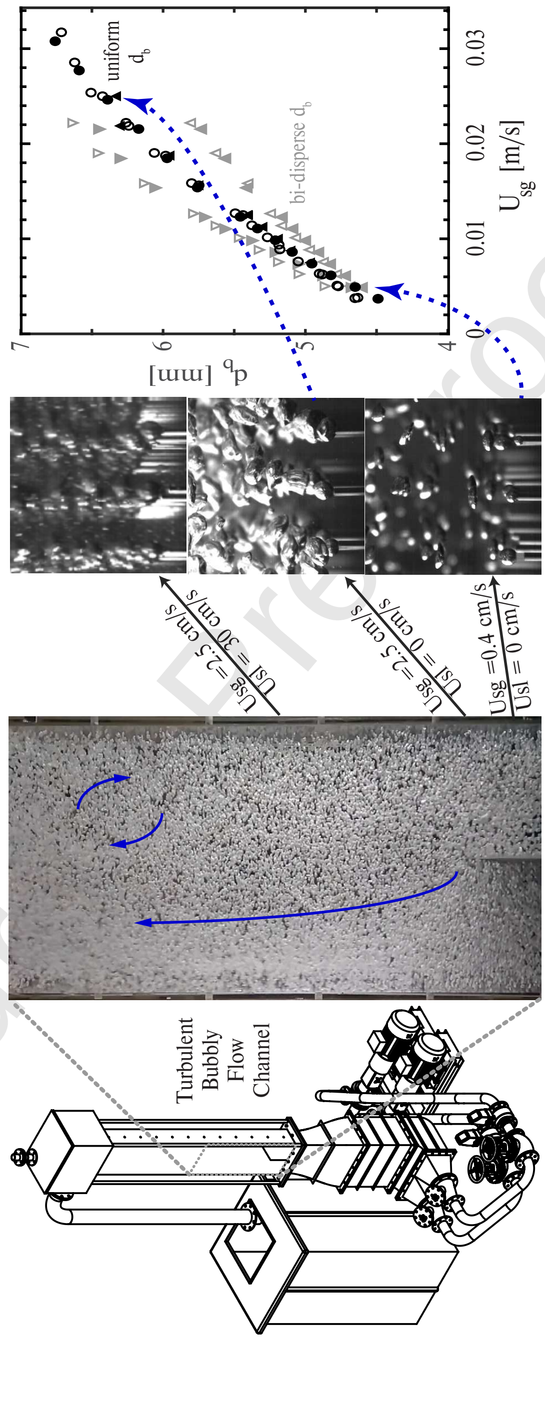
Turbulent Bubbly Flow Channel
Usg = 2.5 cm/s
Usl = 30 cm/s
Usg = 2.5 cm/s
Usl = 0 cm/s
Usg = 0.4 cm/s
Usl = 0 cm/s
uniform d_b
bi-disperse d_b
d_b [mm]
U_sg [m/s]